photonics

Article

Caustics of Non-Paraxial Perfect Optical Vortices Generated by Toroidal Vortex Lenses

Svetlana N. Khonina [1,2,*], Sergey I. Kharitonov [1,2], Sergey G. Volotovskiy [1] and Viktor A. Soifer [1,2]

1 IPSI RAS—Branch of the FSRC "Crystallography and Photonics" RAS, Molodogvardeyskaya 151, 443001 Samara, Russia; prognoz@ipsiras.ru (S.I.K.); sv@ipsiras.ru (S.G.V.); soifer@ssau.ru (V.A.S.)
2 Samara National Research University, Moskovskoye Shosse 34, 443086 Samara, Russia
* Correspondence: khonina@ipsiras.ru; Tel./Fax: +7(846)332-56-20

Abstract: In this paper, we consider the comparative formation of perfect optical vortices in the non-paraxial mode using various optical elements: non-paraxial and parabolic toroidal vortex lenses, as well as a vortex axicon in combination with a parabolic lens. The theoretical analysis of the action of these optical elements, as well as the calculation of caustic surfaces, is carried out using a hybrid geometrical-optical and wave approach. Numerical analysis performed on the basis of the expansion in conical waves qualitatively confirms the results obtained and makes it possible to reveal more details associated with diffraction effects. Equations of 3D-caustic surfaces are obtained and the conditions of the ring radius dependence on the order of the vortex phase singularity are analyzed. In the non-paraxial mode, when small light rings (several tens of wavelengths) are formed, a linear dependence of the ring radius on the vortex order is shown. The revealed features should be taken into account when using the considered optical elements forming the POV in various applications.

Keywords: caustics; perfect optical vortices; toroidal vortex lens

Citation: Khonina, S.N.; Kharitonov, S.I.; Volotovskiy, S.G.; Soifer, V.A. Caustics of Non-Paraxial Perfect Optical Vortices Generated by Toroidal Vortex Lenses. *Photonics* **2021**, *8*, 259. https://doi.org/10.3390/photonics8070259

Received: 26 May 2021
Accepted: 29 June 2021
Published: 5 July 2021

1. Introduction

Recently, the attention of researchers has been attracted by the "perfect" optical vortices (POVs) having a ring radius independent of its vortex number [1–4]. It is well known that classical beams such as Laguerre–Gaussian beams [5–8] and higher-order Bessel beams [9–13] have a central light ring, the size of which is varied with the vortex number. This feature may be undesirable in some applications, for example, when coupling different vortex beams into a fiber with a fixed annular profile [14]. Therefore, the main advantage of POVs over other vortex beams is precisely in the fixed radius of the light ring. Note that recently, various modifications of POVs have appeared, which do not only have a ring structure. For example, elliptical POVs [14–18] in the form of different curves [19–23] and arrays [24–28], POVs with fractional optical vortex [29,30], as well as vector POVs [31–36].

POVs are also used for optical capture and manipulation of microparticles [2,3,37,38] for free-space and underwater optical communication [39–41], for high-resolution plasmonic-structured illumination microscopy [42], in the study of the noncollinear interaction of photons having orbital angular momentum (OAM) in spontaneous parametric down-conversion processes [43], for laser surface structuring [44], and for rotation speed detection of a spinning object based on the rotational Doppler effect [45].

As a rule, the Fourier transformation of Bessel beams or lens-axicon doublets [4,43,46–49] is used to generate such optical beams. In Reference [49], a comparison of POV generation by means of different elements was investigated as follows: using a combination of a lens with an amplitude-phase element with a transmission function proportional to a Bessel function, an optimal phase element with a transmission equal to the sign function of a Bessel function, and a spiral axicon. In fact, these elements are similar, since the axicon is often used to generate Bessel beams [50–52]. A different approach for POV generation was suggested in [26,27] using curved fork gratings.

In this paper, we consider another type of optical element, namely a toroidal lens that corresponds to a non-paraxial lens with radial displacement. The toroidal lens, instead of focusing to a point, focuses the incident radiation into a light ring [53,54]. Thus, the toroidal lens acts similarly to a lens-axicon doublet; however, it has certain advantages since it avoids the aberration problems associated with axicon's tip fabrication [55]. Recently, the attention of researchers has been attracted by the toroidal wave front, which is studied in both the framework of the paraxial wave theory [56] and using the geometrical-optical approach [57,58].

The vortex toroidal lens, as well as the vortex axicon combined with a classic lens, allows for the formation of POVs.

Note, if the ring formed in the focal plane has a small radius, then at large orders of the optical vortex, the POV ceases to be "perfect". It was shown in [59] that for a POV there is a dependence on the order of the optical vortex, especially for optical systems with a low numerical aperture. A similar effect was noted in another work [60].

In this paper, we consider the formation of POV in a non-paraxial mode using toroidal vortex lenses, as well as a vortex axicon in combination with a parabolic lens. The theoretical analysis of the action of these optical elements is carried out on the basis of a hybrid geometrical-optical and wave approach [20,60–62]. The asymptotic method for calculating the Kirchhoff integral is based on the geometric-optical approach with a finite (non-zero) ray thickness. This makes it possible to detect not only geometrical-optical caustics, but also areas of high intensity. Non-paraxial numerical analysis performed on the basis of the expansion in conical waves [63–65] qualitatively confirms the results obtained and makes it possible to reveal more details associated with diffraction effects. Equations of 3D-caustic surfaces are obtained and the conditions for the dependence of the ring radius on the order of the vortex phase singularity are analyzed. The obtained results can be useful in various applications using non-paraxial POVs, such as optical trapping and manipulation, vortex-based multiplexing, and laser structuring.

2. Parametric System of Equations for Calculating a 3D-Caustic Surface

In optics, a caustic is the envelope of light rays reflected or refracted by a curved surface or object [66,67]. The main property of caustic surfaces (or lines) is that near these surfaces the intensity of the light field increases sharply (in the approximation of geometric optics, the intensity tends to infinity) [68,69].

Caustics connected with a curvature of the filed wavefront provide understanding to how the light redistribution evolves [70–73]. Therefore, caustics are used to analyze the features of structured laser beams, such as non-diffracting beams of various types [74–79], generalized Gaussian beams [80,81], accelerating and autofocusing beams [82–86], and vortex beams [20,61,62,87].

A general representation of the caustic surface was obtained for vortex optical elements, the eikonal function of which can be represented in a separable form:

$$\Phi(\rho,\theta) = P(\rho) + \frac{m}{k}\theta \tag{1}$$

where (ρ,θ) are polar coordinates, $k = 2\pi/\lambda$ is the wavenumber of laser radiation with the wavelength λ, and m is the order of the vortex phase singularity.

Calculation of the Kirchhoff integral by the stationary phase method [20,61,62] leads to a parametric equation for calculating the 3D-caustic surface:

$$\begin{cases} r(\rho) = \sqrt{A^2(\rho) + B^2(\rho)}, \\ \varphi(\rho,\theta) = \theta + \tan^{-1}[B(\rho)/A(\rho)], \\ z(\rho,\theta) = \sqrt{S^2(\rho) + 2\rho\cdot r(\rho)\cos[\theta - \varphi(\rho,\theta)] - \rho^2 - r^2(\rho)}\,. \end{cases} \tag{2}$$

where

$$
\begin{array}{c}
A(\rho) = \rho + P_\rho(\rho)\mathrm{S}(\rho), \\
B(\rho) = \frac{m}{k}\frac{\mathrm{S}(\rho)}{\rho},
\end{array}
\quad (3)
$$

where $P_\rho(\rho)$ is the derivative of the radial term $P(\rho)$ of the eikonal function (1), and the function $\mathrm{S}(\rho)$ is the solution to the quadratic equation:

$$
a\mathrm{S}^2(\rho) + b\mathrm{S}(\rho) + c = 0 \quad (4)
$$

with coefficients determined by the following expressions:

$$
\begin{array}{l}
a = \rho^3 P_\rho(\rho) P_{\rho\rho}(\rho) - \left(\frac{m}{k}\right), \\
b = \rho^3\left[\rho P_{\rho\rho}(\rho) + \left(1 - P_\rho^2(\rho)\right)P_\rho(\rho)\right] + \left(\frac{m}{k}\right)^2\left[2\rho P_\rho(\rho) - \rho^2 P_{\rho\rho}(\rho)\right], \\
c = \rho^4\left[1 - P_\rho^2(\rho)\right] - \left(\frac{m}{k}\right)^2\rho^2.
\end{array}
\quad (5)
$$

where $P_{\rho\rho}(\rho)$ is the second derivative of $P(\rho)$.

As follows from the above expressions, the effect of the vortex singularity is noticeable only if the ratio m / k is not too small, i.e., the value of the optical vortex m is commensurate with the wave number k. For conventional optical elements (several millimeters in size) used for the visible wavelength range, k is quite large (has a value of several thousand); therefore, the effect of the vortex singularity manifests itself only at very large values of m. It is this fact that determines the existence of the "perfect" optical vortices. However, if we consider microelements (several microns in size), then the effect of a vortex singularity with the value of m in several tens is already significant. In this work, for a clear demonstration of this effect, we consider microelements (i.e., elements with a size of several tens of microns).

Further, we use the general formulas of this section to analyze different optical elements, especially those that generate the POV.

3. Caustic Surface for Axisymmetric Optical Elements Forming a Light Ring

Let us first consider axisymmetric optical elements that form an annular intensity distribution in a certain transverse plane. For axisymmetric optical elements ($m = 0$), caustic Equation (2) is simplified [88,89]:

$$
\begin{cases}
r(\rho) = \rho + P_\rho(\rho)\mathrm{S}(\rho), \\
z(\rho) = \sqrt{S^2(\rho) - [\rho - r(\rho)]^2},
\end{cases}
\quad (6)
$$

where $\mathrm{S}(\rho)$ is one of the solutions of quadratic Equation (4):

$$
\begin{array}{l}
S_\pm(\rho) = \frac{-b \pm \sqrt{b^2 - 4ac}}{2a}, \\
a = \rho^3 P_\rho(\rho) P_{\rho\rho}(\rho), \\
b = \rho^3\left[\rho P_{\rho\rho}(\rho) + \left(1 - P_\rho^2(\rho)\right)P_\rho(\rho)\right], \\
c = \rho^4\left[1 - P_\rho^2(\rho)\right].
\end{array}
\quad (7)
$$

After simplifications, instead of Equation (7), we obtain:

$$
S_\pm(\rho) = \frac{-\left[\rho P_{\rho\rho}(\rho) + \left(1 - P_\rho^2(\rho)\right)P_\rho(\rho)\right] \pm \left[\rho P_{\rho\rho}(\rho) - \left(1 - P_\rho^2(\rho)\right)P_\rho(\rho)\right]}{2P_\rho(\rho)P_{\rho\rho}(\rho)}. \quad (8)
$$

One solution in Equation (8) corresponds to an off-axis caustic, and the second one corresponds to the axial caustic.

In particular, the "+" sign corresponds to the off-axis caustic:

$$S_+(\rho) = -\frac{1 - P_\rho^2(\rho)}{P_{\rho\rho}(\rho)} \tag{9}$$

in which the surface is described by the following parametric equation:

$$\begin{cases} r_+(\rho) = \rho + P_\rho(\rho)S_+(\rho) = \rho - \left[1 - P_\rho^2(\rho)\right] P_\rho(\rho) P_{\rho\rho}^{-1}(\rho), \\ z_+(\rho) = \sqrt{S_+^2(\rho) - [\rho - r_+(\rho)]^2} = \left[1 - P_\rho^2(\rho)\right]^{3/2} P_{\rho\rho}^{-1}(\rho). \end{cases} \tag{10}$$

The sign "$-$" corresponds to the axial caustic:

$$S_-(\rho) = -\frac{\rho}{P_\rho(\rho)} \tag{11}$$

in which surface is described by the following parametric equation:

$$\begin{cases} r_-(\rho) = \rho + P_\rho(\rho)S_-(\rho) = \\ \qquad = \rho - \rho P_\rho^{-1}(\rho) P_\rho(\rho) = 0\,, \\ z_-(\rho) = \sqrt{S_-^2(\rho) - [\rho - r_-(\rho)]^2} = \\ \qquad = \sqrt{\left[\rho P_\rho^{-1}(\rho)\right]^2 - \rho^2} = \rho\left[1 - P_\rho^2(\rho)\right]^{1/2} P_\rho^{-1}(\rho)\,. \end{cases} \tag{12}$$

It clearly follows from Equation (12) that the axial caustic is located on the optical axis, since its radius $r_-(\rho) = 0$. Note that there are no caustics when $1 - P_\rho^2(\rho) < 0$.

The convenience of the obtained Expressions (9)–(12) lies in the fact that the construction of caustic surfaces is sufficient to know the first and second derivatives of the eikonal function.

We further consider specific optical elements below.

3.1. Non-Paraxial Toroidal Lens

A toroidal lens is an optical element that focuses into a ring. The complex transmission function of the toroidal lens focusing into a ring with a radius ρ_0 at a distance $z = f$ is described by the following expression:

$$\tau_{tor}(\rho) = \exp\left(-ik\sqrt{(\rho - \rho_0)^2 + f^2}\right) \tag{13}$$

Obviously, at $\rho_0 = 0$, Expression (13) is reduced to an ordinary non-paraxial lens focusing to a point on the optical axis. Let us obtain analytical expressions for the caustic surface for the toroidal lens (13) using Equations (9)–(12).

Let us write the eikonal function of the optical element (13):

$$\Phi_{tor}(\rho) = P(\rho) = -\sqrt{(\rho - \rho_0)^2 + f^2} \tag{14}$$

and write out the first and second derivatives:

$$\begin{aligned} P_\rho(\rho) &= -\frac{(\rho-\rho_0)}{\sqrt{(\rho-\rho_0)^2+f^2}} = \frac{(\rho-\rho_0)}{P(\rho)}, \\ P_{\rho\rho}(\rho) &= -\frac{f^2}{\left((\rho-\rho_0)^2+f^2\right)^{3/2}} = \frac{f^2}{P^3(\rho)}. \end{aligned} \tag{15}$$

Then, for an off-axis caustic, we obtain:

$$\begin{cases} r_{tor,+}(\rho) = \rho - \left[1 - P_\rho^2(\rho)\right] P_\rho(\rho) P_{\rho\rho}^{-1}(\rho) = \rho_0, \\ z_{tor,+}(\rho) = \left[1 - P_\rho^2(\rho)\right]^{3/2} P_{\rho\rho}^{-1}(\rho) = f, \end{cases} \tag{16}$$

It follows from Expression (16) that the off-axis caustic is a ring with the radius ρ_0 at the focal length f. At $\rho_0 = 0$ the caustic consists of one point on the axis at the focal length.

For axial caustics:

$$\begin{cases} r_{tor,-}(\rho) = 0, \\ z_{tor,-}(\rho) = \rho\left[1 - P_\rho^2(\rho)\right]^{1/2} P_\rho^{-1}(\rho) = \frac{f\rho}{(\rho - \rho_0)}, \end{cases} \tag{17}$$

Note that axial caustics are formed when $\rho > \rho_0$.

Figure 1 shows the results of diffraction of a plane beam by a toroidal lens and the formation of a ring in the focal plane for the following parameters: $\lambda = 633$ nm, $\rho_0 = 30$ µm, and $f = 100$ µm.

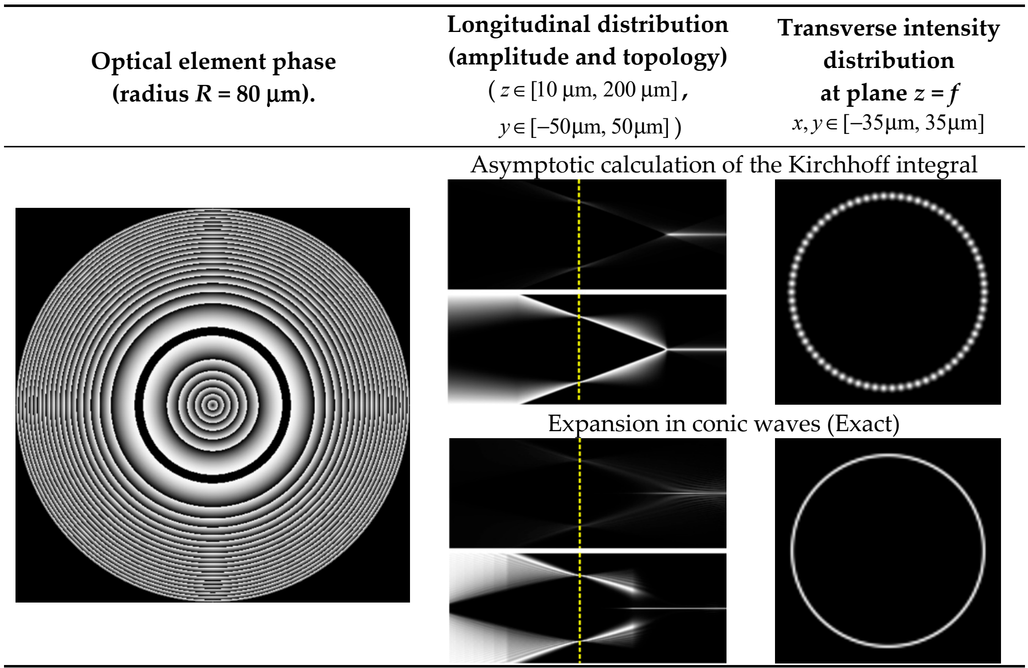

Figure 1. Calculation of the formation of a field by the toroidal lens (13) under illumination with a plane beam.

The calculation was performed using the asymptotic method for calculating the Kirchhoff integral [88,89]. The asymptotic method for calculating the Kirchhoff integral is based on the geometric-optical approach with a finite (non-zero) ray thickness. This makes it possible to detect not only geometrical-optical caustics, but also areas of high intensity. This is a feature of the hybrid approach of the asymptotic calculation method. For comparison, the results obtained by the method of expansion in conical waves [63–65] are also shown. This method is accurate and takes into account diffraction effects.

To visualize the formation of high-intensity surfaces that correspond to caustic surfaces, Figure 1 shows longitudinal distribution of generated field: amplitude (root of intensity) to show distribution in more detail and topology (logarithmic scale of intensity) to show picture analogs to ray tracing. The color matching for all pictures in the gray palette is as follows: black color for the minimal (zero) value and white color for the maximal values.

As can be seen from Figure 1, the off-axis caustic provides the formation of a ring in the focal plane (marked in Figure 1 by yellow vertical line), and the axial caustic is responsible for the appearance of a light line on the optical axis, which is formed at a distance $z > f$. Note that the structural (caustic) features of the generated field, especially its longitudinal distribution, are more clearly defined using the asymptotic-geometric approach, but the fine details and distribution in the focal plane are correctly shown by the method of expansion in conical waves. Thus, each of the methods allows one to focus on various features of the generated fields. It is known that the use of a Gaussian illuminating beam makes it possible to smooth out diffraction effects and emphasize structural features. Figure 2 shows the results of calculating the formation of a light ring under illumination of the toroidal lens (shown in Figure 1) by Gaussian beams $\exp(-r^2/\sigma^2)$ of various radius σ.

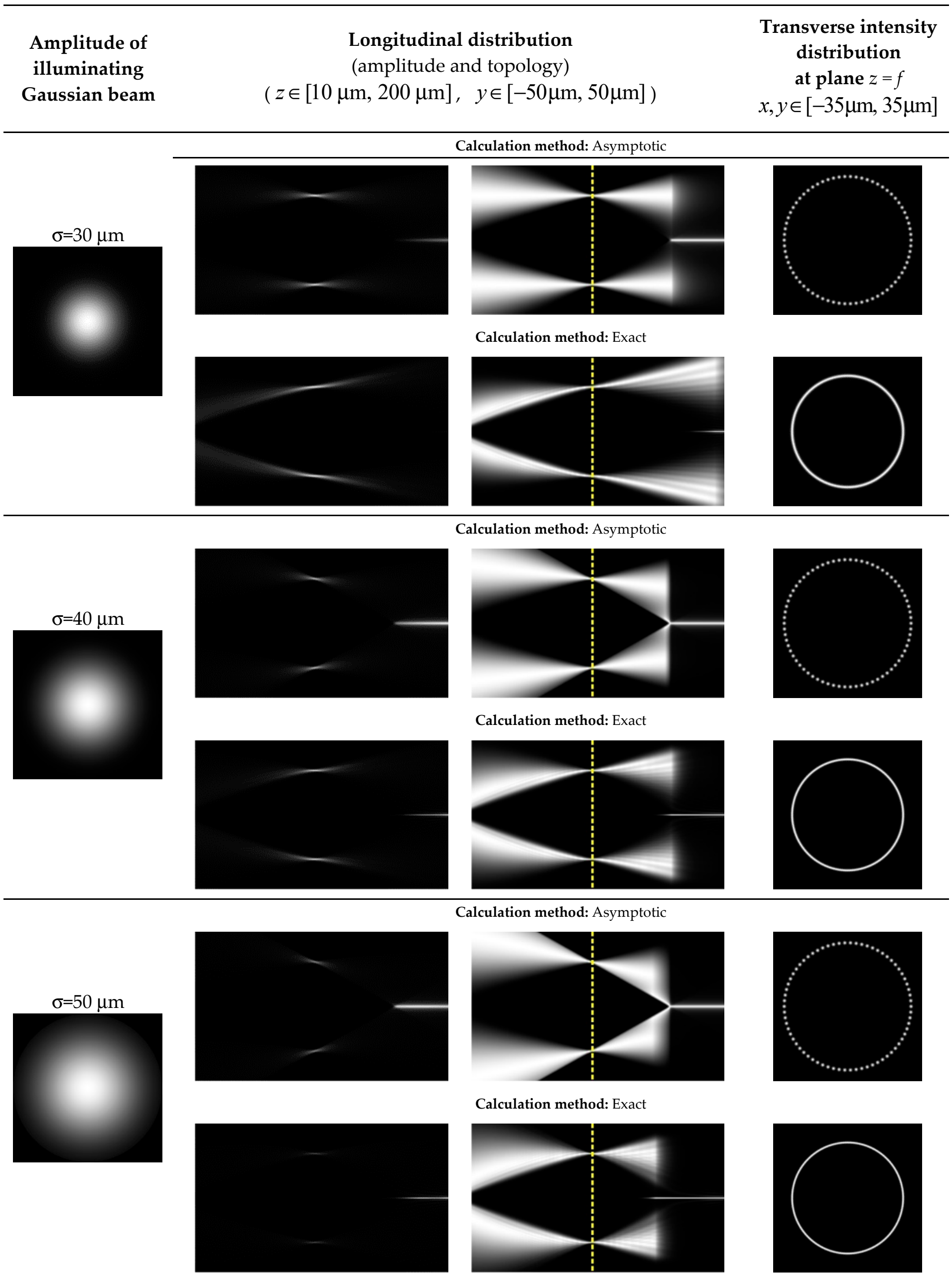

Figure 2. Calculation of the formation of a field by the toroidal lens (13) under illumination with a Gaussian beam.

Figure 2 shows that using the asymptotic method we obtain the structure of the field practically the same for various size of the illuminating beam. The exact method (expansion in conical waves) shows noticeable differences for a small Gaussian beam ($\sigma = 30$ µm) when the field is paraxial, and a larger Gaussian beam ($\sigma = 50$ µm) when the field is already non-paraxial. Note that, in the latter case, the beam structure calculated by both methods is very similar.

Note that Expressions (16)–(17), which predict the existence of regions with high intensity, were obtained from the geometric optics approximation. In this case, these areas are concentrated near the ring and on the optical axis. Thus, in the geometrical optics approximation, there should be infinite intensity in these regions. However, light diffraction introduces significant changes in the intensity pattern. In particular, the calculation (by exact method) shows the presence of other regions of increased intensity. In addition, the illuminating beam has an influence, which is difficult to take into account in the framework of geometric optics. A certain compromise in this case is achieved by using the asymptotic, in which the transverse size of the beam has a non-zero thickness. In this case, the energy is redistributed in the vicinity of the caustic and its brightness decreases.

3.2. Parabolic Toroidal Lens

The complex transmission function of a parabolic toroidal lens can be obtained from Expression (13) provided that the focal length f is large enough:

$$\tau_{tor}(\rho) = \exp\left(-ikf\sqrt{1+(\rho-\rho_0)^2/f^2}\right) \approx \exp\left(-ikf\left[1+\frac{(\rho-\rho_0)^2}{2f^2}\right]\right). \tag{18}$$

Omitting the constant phase factor $\exp(-ikf)$, we obtain the following expression for the parabolic toroidal lens:

$$\tau_{ptor}(\rho) = \exp\left(-ik\frac{(\rho-\rho_0)^2}{2f}\right) \tag{19}$$

The eikonal function for the parabolic toroidal lens:

$$\Phi_{ptor}(\rho) = P(\rho) = -\frac{(\rho-\rho_0)^2}{2f} \tag{20}$$

The first and second derivatives in this case:

$$P_\rho(\rho) = -\frac{(\rho-\rho_0)}{f}, \quad P_{\rho\rho}(\rho) = -\frac{1}{f}. \tag{21}$$

An off-axis caustic surface is described by:

$$\begin{cases} r_{ptor,+}(\rho) = \rho - \left[1-P_\rho^2(\rho)\right]P_\rho(\rho)P_{\rho\rho}^{-1}(\rho) = \rho_0 + \frac{(\rho-\rho_0)^3}{f^2}, \\ z_{ptor,+}(\rho) = \left[1-P_\rho^2(\rho)\right]^{3/2}P_{\rho\rho}^{-1}(\rho) = -f\left[1-\frac{(\rho-\rho_0)^2}{f^2}\right]^{3/2}. \end{cases} \tag{22}$$

It follows from Expression (22) that now the off-axis caustic is a certain surface near the ring with radius ρ_0. When $\rho_0 = 0$, the parabolic toroidal lens transforms into an ordinary parabolic lens, the off-axis caustic of which is a "caustic beak" surface [61,90]. This is the main difference between a parabolic (paraxial) lens and a non-paraxial lens.

For the axial caustic, a more complex expression than (17), is also obtained:

$$\begin{cases} r_{ptor,-}(\rho) = 0, \\ z_{ptor,-}(\rho) = \rho\left[1-P_\rho^2(\rho)\right]^{1/2}P_\rho^{-1}(\rho) = -\left[f^2-(\rho-\rho_0)^2\right]^{1/2}\frac{\rho}{(\rho-\rho_0)}. \end{cases} \tag{23}$$

Figure 3 shows the simulation results obtained using an asymptotic and accurate calculation of the plane beam diffraction by the parabolic toroidal lens (19) with the same parameters as for non-paraxial toroidal lens (13) in Section 3.1.

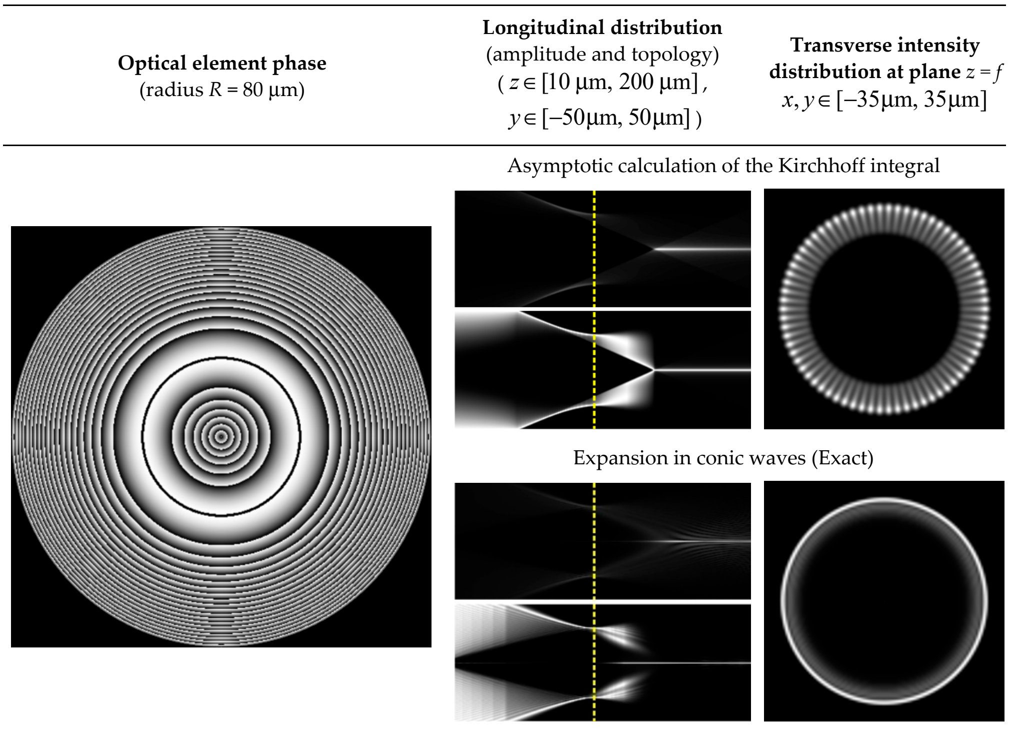

Figure 3. Calculation of the formation of a field by the parabolic toroidal lens (13) under illumination with a plane beam.

As can be seen from a comparison of the simulation results shown in Figures 1 and 3, the non-paraxial toroidal lens (13) produces a narrower (and therefore brighter) ring of light than the parabolic lens (19). The appearance of off-axis caustics for these optical elements is also noticeably different (see Figure 4): for a non-paraxial toroidal lens, this is a thin ring (the graph of the radial section is the red colored point in Figure 4a), and for a parabolic toroidal lens, the caustic surface becomes more complex (3D view is shown in Figure 4b). This is a "caustic beak" distribution, which is characteristic of the caustic of a parabolic wavefront [90]. In contrast to focusing to an axial point considered in the work [90], the wavefront considered in our paper is also parabolic, but with a radial displacement. Therefore, a characteristic distribution is observed along the ring (Figure 4b).

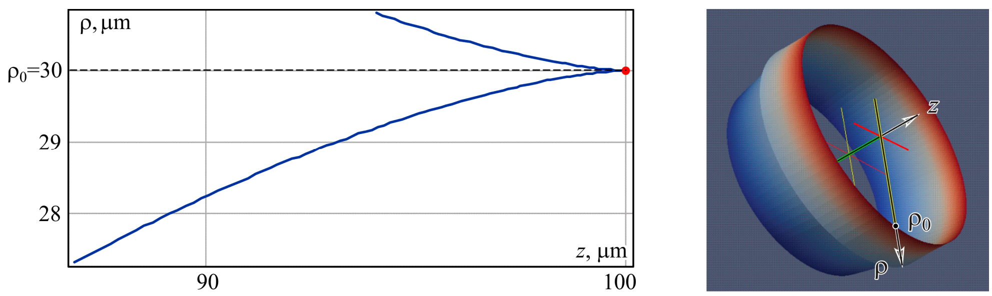

(**a**) (**b**)

Figure 4. Off-axis caustics: (**a**) comparative graphs of radial sections for non-paraxial (red point) and parabolic (blue line) toroidal lens and (**b**) 3D view of caustics.

3.3. Axicon-Lens Doublet

The complex transmission function of parabolic toroidal lens (19) can be represented in the following form:

$$\tau_{ptor}(\rho) = \exp\left(-ik\frac{(\rho-\rho_0)^2}{2f}\right) = \exp\left(-ik\frac{{\rho_0}^2}{2f}\right)\exp\left(ik\frac{\rho_0}{f}\rho\right)\exp\left(-ik\frac{\rho^2}{2f}\right). \quad (24)$$

Omitting the constant phase factor $\exp\left[-ik\left({\rho_0}^2/2f\right)\right]$, we obtain a doublet from the scattering axicon and the converging parabolic lens:

$$\tau_{lax}(\rho) = \exp\left(ik\frac{\rho_0}{f}\rho\right)\exp\left(-ik\frac{\rho^2}{2f}\right) \quad (25)$$

The eikonal function for doublet (25) is as follows:

$$\Phi_{lax}(\rho) = P(\rho) = \frac{\rho_0}{f}\rho - \frac{\rho^2}{2f} \quad (26)$$

The first and second derivatives in this case:

$$P_\rho(\rho) = \frac{\rho_0-\rho}{f}, \quad P_{\rho\rho}(\rho) = -\frac{1}{f}. \quad (27)$$

As can be seen from a comparison of Equations (21) and (27), a parabolic toroidal lens and an axicon doublet with a parabolic lens are completely analogous.

4. Caustic Surface for Vortex Optical Elements Forming a Light Ring

The results of the previous section showed that axisymmetric optical elements have two types of caustics—axial and off-axis. It was shown in [20,61,62] that the presence of a vortex phase singularity leads to a fundamental change in the axial caustic—it becomes off-axis. Thus, vortex optical elements form two off-axis caustics, which can change the distribution of the light field. This includes changing the radius of the light ring, i.e., violate the basic property of POVs. To investigate this, let us write Equation (2) for vortex caustic surfaces taking into account the factorization of the angular dependence:

$$\begin{cases} r(\rho) = \sqrt{A^2(\rho)+B^2(\rho)}, \\ z(\rho) = \sqrt{S^2(\rho)+2\rho\cdot r(\rho)\cos\{\tan^{-1}[B(\rho)/A(\rho)]\}-\rho^2-r^2(\rho)}. \end{cases} \quad (28)$$

As can be seen from Equation (28), the presence of a vortex phase (i.e., $m \neq 0$) does not change the axisymmetric character of caustic surfaces but does change their shape.

Using the relation $\cos\left[\tan^{-1}(x)\right] = \left(1+x^2\right)^{-1/2}$ instead of Equation (28), we obtain:

$$\begin{cases} r(\rho) = \sqrt{A^2(\rho)+B^2(\rho)}, \\ z(\rho) = \sqrt{S^2(\rho)+2\rho\cdot r(\rho)\left\{1+[B(\rho)/A(\rho)]^2\right\}^{-1/2}-\rho^2-r^2(\rho)}. \end{cases} \quad (29)$$

In the general case, Equation (29) for caustic surfaces is rather difficult to analyze. To get some analytical estimates, we consider two cases: small and large values of m/k.

When m/k is small ($m/k < 1$), then $B(\rho) << A(\rho)$. In this case, using the expansion of the root in the Taylor series instead of Equation (29), we can write:

$$\begin{cases} r(\rho) = A(\rho)\sqrt{1+\left(\frac{B(\rho)}{A(\rho)}\right)^2} \approx A(\rho)+\frac{B^2(\rho)}{2A(\rho)}, \\ z(\rho) = \sqrt{S^2(\rho)\pm 2\rho r(\rho)\left[1-\frac{1}{2}\left(\frac{B(\rho)}{A(\rho)}\right)^2\right]-\rho^2-r^2(\rho)}, \end{cases} \quad (30)$$

where $A(\rho) = \rho + P_\rho(\rho)S(\rho)$, $B(\rho) = mS(\rho)/k\rho$, and the "+" sign corresponds to the case when $A(\rho) > 0$, and the "−" sign when $A(\rho) < 0$.

As can be seen from Equation (30), the caustic radius changes even at small orders of the vortex singularity m ($m/k < 1$):

$$r(\rho) \approx A(\rho) + \Delta(\rho), \tag{31}$$

where $A(\rho)$ corresponds to the radius of the original caustic, and the addition is described by Equation (32):

$$\Delta(\rho) = \frac{m^2 S^2(\rho)}{2(k\rho)^2\left[\rho + P_\rho(\rho)S(\rho)\right]} \tag{32}$$

As seen from Equation (32), the changes have a quadratic dependence on the order of the vortex singularity m. However, they will be very minor as long as the ratio m/k is small.

If the ratio m/k is large ($m/k >> 1$), then the caustic radius takes on a completely different form:

$$r(\rho) \approx B(\rho) + \frac{A^2(\rho)}{2B(\rho)} = \frac{mS(\rho)}{k\rho} + \frac{k\rho\left[\rho + P_\rho(\rho)S(\rho)\right]^2}{2mS(\rho)} \tag{33}$$

It is obvious from Equation (33) that, in this case, the radius will grow linearly with increasing order m.

Next, we take a closer look at specific optical elements.

4.1. Non-Paraxial Vortex Toroidal Lens

The complex transmission function of a vortex toroidal lens of order m is described by the following expression:

$$\tau_{tor}(\rho,\theta) = \exp\left(-ik\sqrt{(\rho-\rho_0)^2 + f^2} + im\theta\right) \tag{34}$$

Let us write the eikonal function of the optical element (34) in the form (1):

$$\Phi_{tor}(\rho,\theta) = P(\rho) + \frac{m}{k}\theta = -\sqrt{(\rho-\rho_0)^2 + f^2} + \frac{m}{k}\theta \tag{35}$$

Since the eikonal function of the considered elements is factorized (separable) in radial and angular coordinates, the first and second radial derivatives have the form as in Equation (15).

Let us write out the coefficients of quadratic Equation (4) in explicit form using Expression (5) and taking into account the relation $P^2(\rho) = (\rho-\rho_0)^2 + f^2$:

$$\begin{aligned}
a &= \rho^3 f^2 \tfrac{(\rho-\rho_0)}{P^4(\rho)} - \left(\tfrac{m}{k}\right), \\
b &= \tfrac{\rho^3 f^2}{P^3(\rho)}[\rho + (\rho-\rho_0)] + \tfrac{\rho}{P^3(\rho)}\left(\tfrac{m}{k}\right)^2\left[2(\rho-\rho_0)\left[(\rho-\rho_0)^2 + f^2\right] - \rho f^2\right], \\
c &= \tfrac{\rho^4}{P^2(\rho)} f^2 - \left(\tfrac{m}{k}\right)^2\rho^2.
\end{aligned} \tag{36}$$

Using the coefficients in Equation (36), one can numerically obtain solutions $S_\pm(\rho) = \left(-b \pm \sqrt{b^2 - 4ac}\right)/2a$ for all values of ρ. Note, however, that the presence of a vortex singularity transforms axial caustics into off-axis ones [20,61,62], and, therefore, for a certain range $\rho \in [0, \rho_d]$, the system in Equation (29) will not have a solution. The allowed area is determined from Equation (37):

$$S^2(\rho) + 2\rho \cdot r(\rho)\left\{1 + [B(\rho)/A(\rho)]^2\right\}^{-1/2} > \rho^2 + r^2(\rho) \tag{37}$$

Figure 5 shows the view of off-axis caustics for a non-paraxial vortex toroidal lens (34) at different orders of the vortex phase singularity m. As can be seen, the off-axis caustic instead of a ring becomes a surface of revolution resembling a cone (Figure 5b).

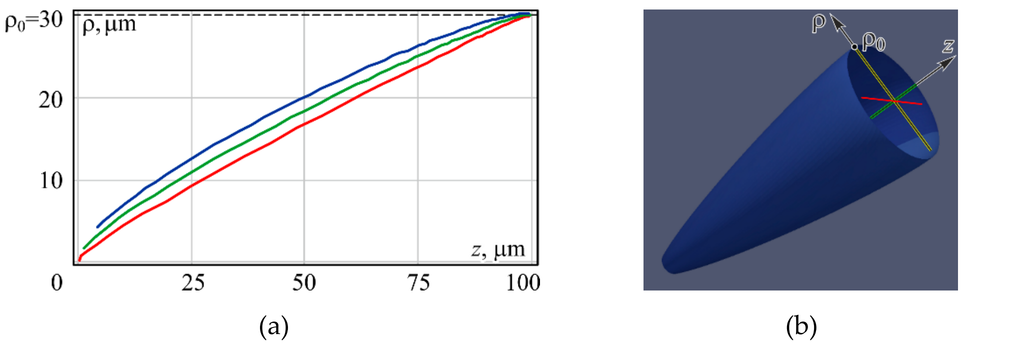

Figure 5. Off-axis caustics for non-paraxial vortex toroidal lens (34): (**a**) comparative graphs of radial sections when m = 1 (red), m = 5 (green), and m = 10 (blue); (**b**) 3D view of the caustic at m = 10.

Figure 6 shows the results of calculating the diffraction of a plane beam by a non-paraxial vortex toroidal lens at $m = 10$. Since the caustics (Figure 5) are obtained in the geometrical-optical approximation, the diffraction theory does not guarantee the maximum intensity on the caustic surface. However, we can see a peculiarity (Figure 6): this surface is the boundary between light and shadow, which is clearly seen in the topology (logarithmic scale of intensity), which shows details in analogy to ray tracing.

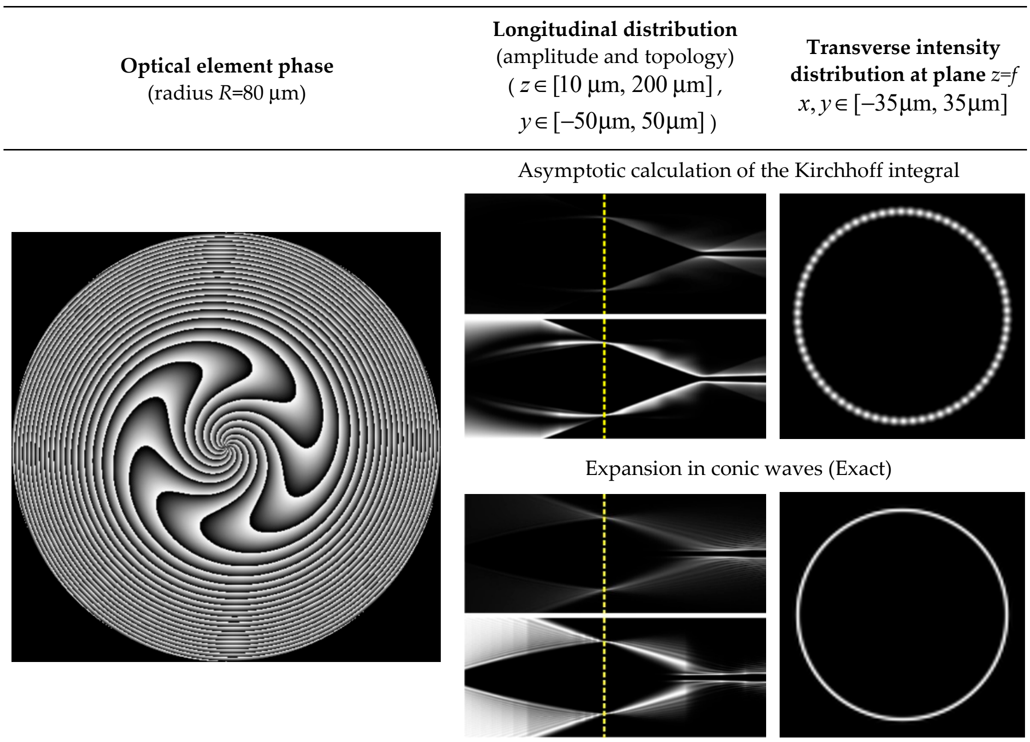

Figure 6. Calculation of the field formation by a vortex (m = 10) toroidal lens (34) when illuminated by a plane beam.

The caustic surface becomes more pronounced when a Gaussian beam is used as an illuminating beam (Figure 7). When illuminated by a Gaussian beam, the geometric caustics are more noticeable for two reasons. First, the caustic is formed by the rays coming from the central part, and the Gaussian beam has the highest intensity precisely in the center. Second, in the case of a Gaussian beam, the diffraction effects are minimal. As the radius of the Gaussian beam increases, the diffraction effect associated with the edge of the aperture increases. Within the framework of the geometric theory of diffraction, in this case, "diffraction" rays arise [91,92] and the formation of caustics of "diffraction" rays is possible.

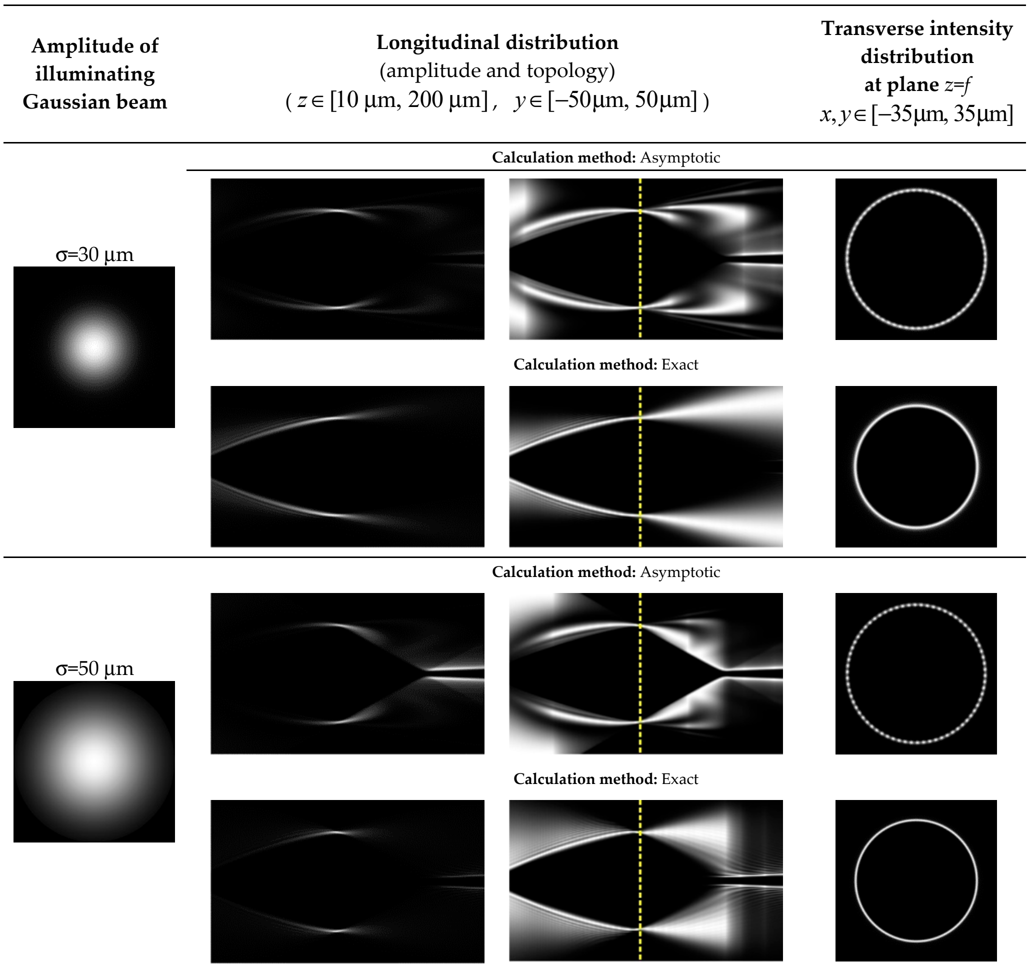

Figure 7. Calculation of the field formation by a vortex (m = 10) toroidal lens (34) when illuminated by Gaussian beam.

4.2. Analysis of the Effect of the Vortex Phase in a Non-Paraxial Mode

In this paper, we consider the formation of POV not only in the non-paraxial mode, but also for focal light rings with a small radius (several tens of wavelengths). Note that if the ring formed in the focal plane has a small radius, then at large orders of the optical vortex m POV, the POV ceases to be “perfect”.

In Reference [59], it was shown that in order to satisfy the condition for the formation of a POV, the radius of the ring should be:

$$\rho_0 \geq \rho_c = \frac{|m|}{k \cdot NA} \tag{38}$$

where NA is the numerical aperture of the optical system.

In the paraxial approximation $NA \approx R/f$, therefore, using Equation (38), it is possible to estimate the maximum value of the vortex order $|m_{\max}|$, at which the condition for the formation of the POV will be met:

$$|m_{\max}| \leq \frac{kR\rho_0}{f} \tag{39}$$

For the non-paraxial regime considered in our work, the numerical aperture is determined by the following equation:

$$NA = \sin\left[\tan^{-1}(R/f)\right] \tag{40}$$

For the parameters used in the calculations ($\lambda = 0.633$ μm, $\rho_0 = 30$ μm, $f = 100$ μm, $R = 80$ μm) using Equation (39) we estimate $|m_{\max}| \leq 238$ ($NA \approx 0.8$), and using Equation (40) and Equation (38), we estimate $|m_{\max}| \leq 184(NA \approx 0.62)$. Both values are quite large.

Figure 8 shows the results of modeling by the method of expansion in conical waves, and Figure 9 shows comparative graphs of the cross-sections of the intensity of the light ring in the focal plane at different values of m. To define the radius of the ring we estimate position of maximal intensity $\rho_{\max}$ (Figure 9). Thus, we calculate: $\rho_{\max} = 29.99$ μm (m = 0), $\rho_{\max} = 29.99$ μm (m = 1), $\rho_{\max} = 30.08$ μm (m = 5), $\rho_{\max} = 30.17$ μm (m = 10), $\rho_{\max} = 30.37$ μm (m = 20), $\rho_{\max} = 31.56$ μm (m = 50), and $\rho_{\max} = 34.34$ μm (m = 100).

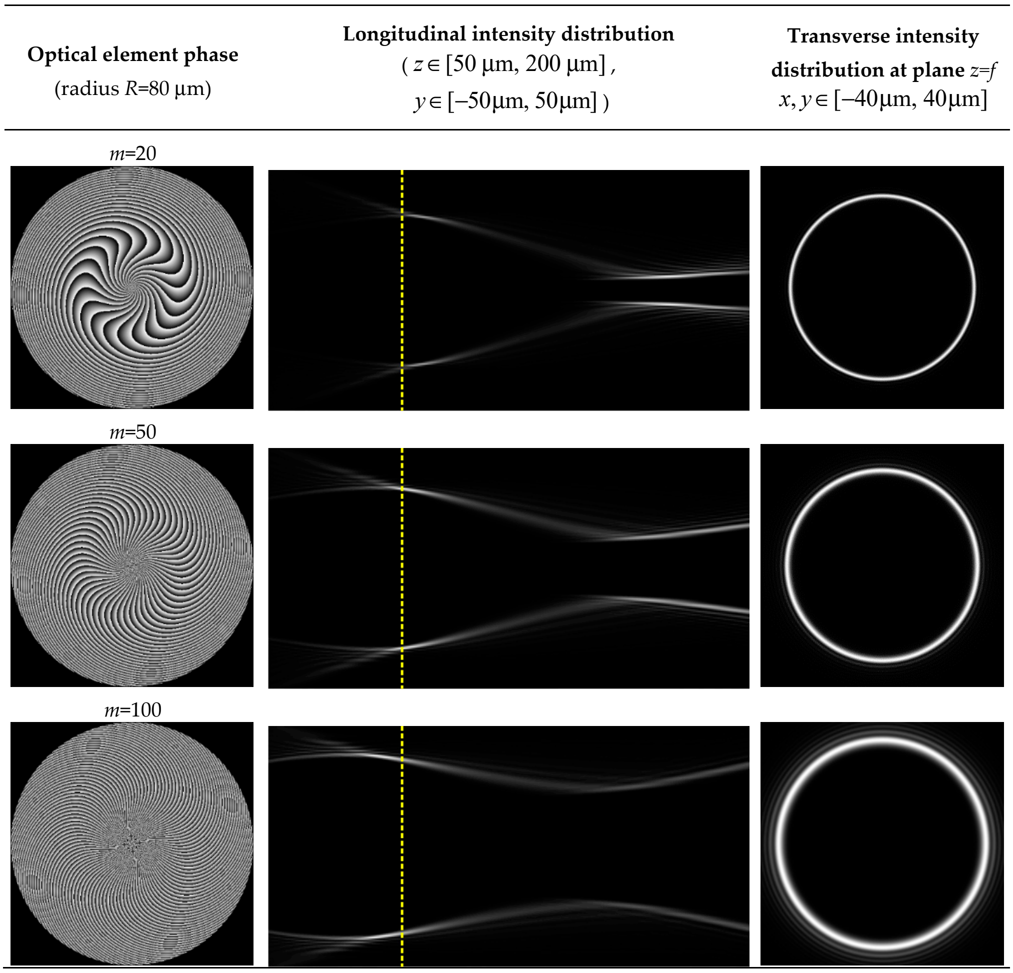

Figure 8. Comparative calculation of the field formation by a non-paraxial vortex toroidal lens (34) for different high-orders of m.

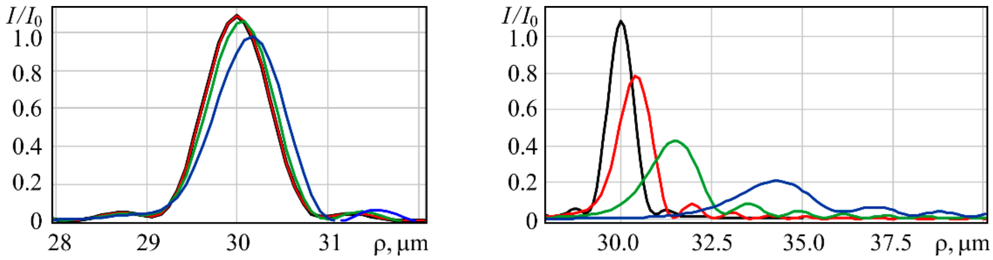

(a) (b)

Figure 9. Graphs of the cross-sections of the intensity of the light ring in the focal plane, formed by a vortex non-paraxial toroidal lens (35) (ρ_0 = 30 µm) for different values of m: (**a**) m = 0 (black), m = 1 (red), m = 5 (green), and m = 10 (blue); (**b**) m = 0 (black), m = 20 (red), m = 50 (green), and m = 100 (blue).

As can be seen from Figures 8 and 9, for large values of the optical vortex number m, the radius of the ring increases significantly, and the violation of POV formation occurs much earlier than predicted by condition (38).

A noticeable increase in the radius of the focal ring for the characteristics under consideration occurs already at $|m| \geq 10$ (Figure 9a,b). Note that the calculation of caustic surfaces also predicts this (Figure 10a).

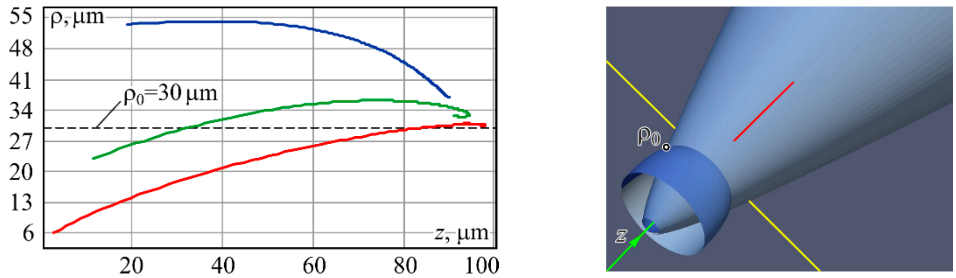

(**a**) (**b**)

Figure 10. Off-axis caustics for a non-paraxial vortex toroidal lens (34): (**a**) comparative graphs of radial sections when m = 20 (red), m = 50 (green), and m = 100 (blue), (**b**) 3D view of caustics (off-axis and axial modification) at m = 100.

The significant sensitivity of non-paraxial POVs to an increase in the optical vortex number m is associated with the non-paraxial nature of the optical elements under consideration. This behavior is explained by the analysis performed in Section 4, where it is shown that for small orders of the vortex phase singularity m ($m < 2\pi/\lambda$), the increase in the ring radius will be negligible, and for large values of m ($m >> 2\pi/\lambda$), the ring will grow linearly with m. For the parameters considered in the calculations, the wave number $k = 2\pi/\lambda \approx 10\,\mu m^{-1}$. Therefore, for $|m| < 10$, the radius of the ring practically does not change (Figure 9a), and for $|m| \geq 10$, there is a linear increase in the radius with increasing m (Figure 9b).

4.3. Parabolic Vortex Toroidal Lens

The complex transmission function of a parabolic vortex toroidal lens has the form:

$$\tau_{ptor}(\rho,\theta) = \exp\left(-ik\frac{(\rho-\rho_0)^2}{2f} + im\theta\right) \tag{41}$$

and the eikonal function is as follows:

$$\Phi_{ptor}(\rho,\theta) = P(\rho) + \frac{m}{k}\theta = -\frac{(\rho-\rho_0)^2}{2f} + \frac{m}{k}\theta \tag{42}$$

Taking into account that the first and second derivatives are the same as in Equation (21), we write down the coefficients of quadratic Equation (4) in the explicit form:

$$\begin{aligned} a &= \rho^3 \tfrac{(\rho-\rho_0)}{f^2} - \left(\tfrac{m}{k}\right), \\ b &= \rho^3\left[-\tfrac{\rho}{f} - \left(1 - \left[\tfrac{(\rho-\rho_0)}{f}\right]^2\right)\tfrac{(\rho-\rho_0)}{f}\right] + \left(\tfrac{m}{k}\right)^2\left[-2\rho\tfrac{(\rho-\rho_0)}{f} + \tfrac{\rho^2}{f}\right], \\ c &= \rho^4\left(1 - \left[\tfrac{(\rho-\rho_0)}{f}\right]^2\right) - \left(\tfrac{m}{k}\right)^2\rho^2. \end{aligned} \tag{43}$$

In the paraxial case, the analysis of the caustic surface in the presence of a phase vortex singularity is not simplified and, in fact, corresponds to the expressions obtained at the beginning of Section 4. In this section, we consider numerical calculations in order to clarify the effect of the number m on the formation of the focal ring.

Figure 11 shows the caustics of a parabolic vortex toroidal lens (41) for different orders of m. As can be seen, the effect of the vortex phase singularity at small values of m is insignificant (as well as for the non-paraxial lens considered in Sections 4.1 and 4.2); therefore, we consider in more detail the effect of high orders of m.

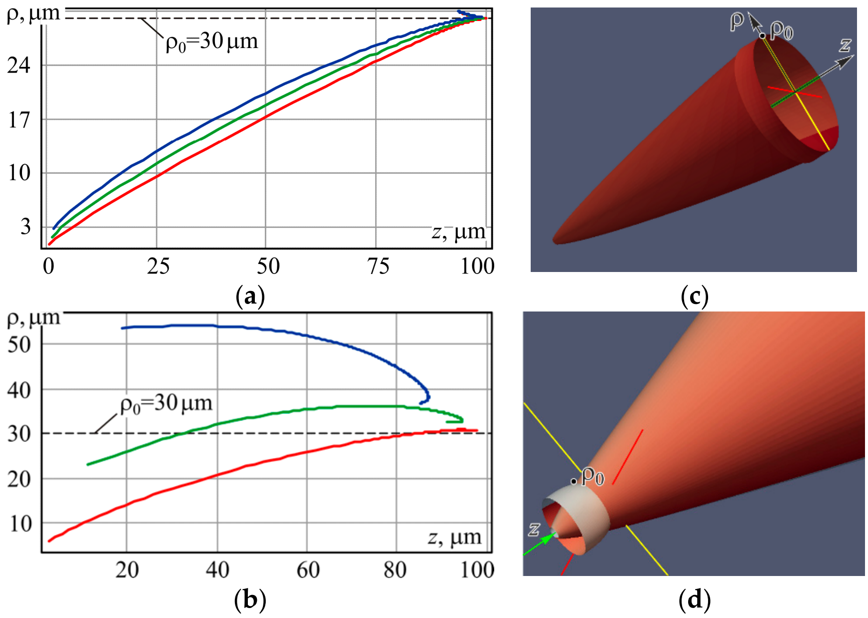

Figure 11. Off-axis caustics for a parabolic vortex toroidal lens (41): comparative graphs of radial sections with (**a**) m = 1 (red), m = 5 (green), and m = 10 (blue); (**b**) m = 20 (red), m = 50 (green), and m = 100 (blue); as well as a 3D view of caustics with (**c**) m = 10 and (**d**) m = 100.

Figure 12 shows the results of modeling of diffraction of a plane beam on a parabolic vortex toroidal lens (41) by the method of expansion in conical waves with the same parameters that were used in Section 3.2 for a non-paraxial lens. Comparison of the calculation results (Figures 8 and 12) shows that at high orders of m ($m/k >> 1$), not only is a linear increase in the radius of the ring in the focal plane observed, but also its noticeable spreading. This is due to the displacement of the plane of formation of the ring closer to the plane of the element, which is clearly seen in the longitudinal intensity patterns (Figure 12, red line). This effect is less pronounced for a non-paraxial vortex toroidal lens (34) than for the element (41). This fact must be taken into account when using the considered optical elements that form the POV in various applications.

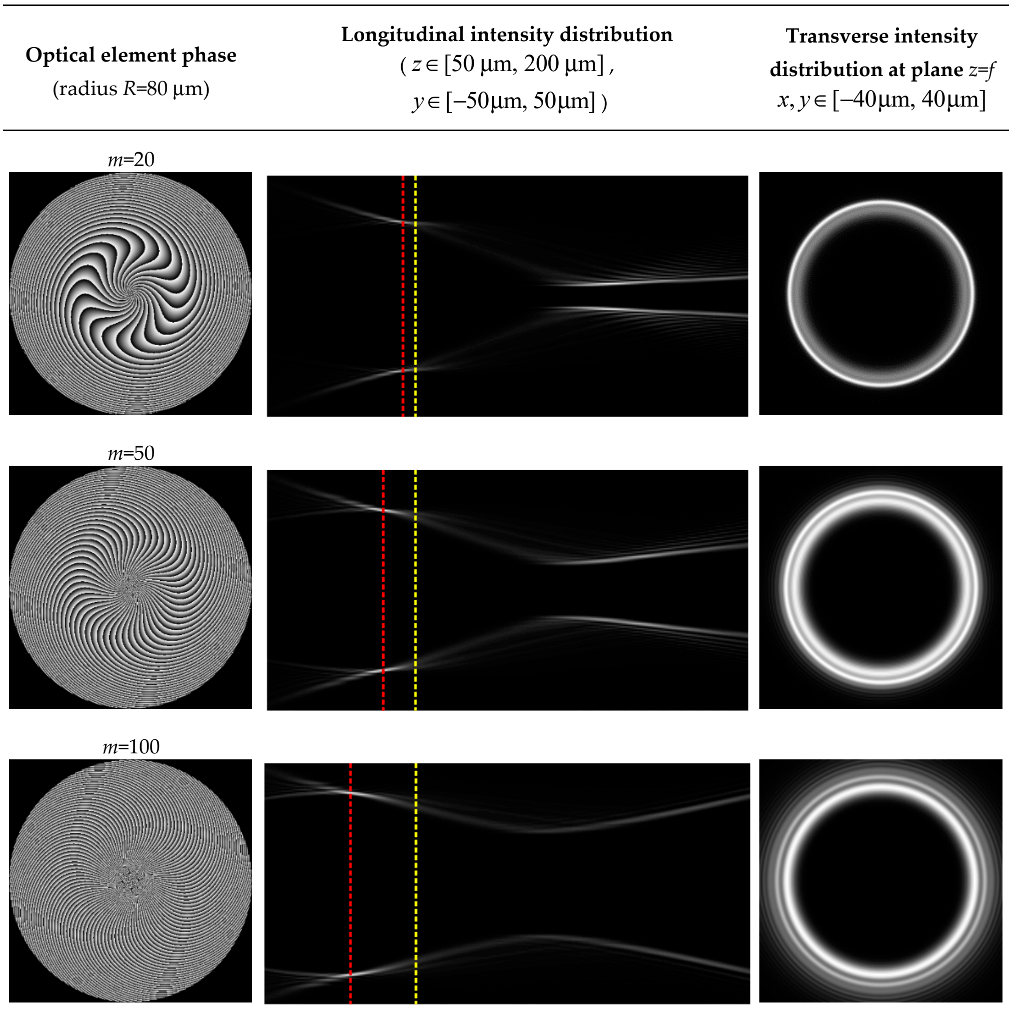

Figure 12. Comparative calculation of the field formation by a parabolic vortex toroidal lens (41) for different high-order m: the yellow line shows the position of the focal plane, and the red line shows the position of the plane of maximum intensity.

5. Conclusions

In this work, a theoretical and numerical study of the formation of perfect optical vortices in the non-paraxial mode was carried out using various optical elements: non-paraxial and parabolic toroidal vortex lenses, as well as a vortex axicon in combination with a parabolic lens. The theoretical analysis of the action of these optical elements, as well as the calculation of caustic surfaces, was carried out using the asymptotic method for calculating the Kirchhoff integral, based on the geometric-optical approach with a finite (non-zero) ray thickness. This makes it possible to detect not only geometrical-optical caustics, but also regions with high intensity, i.e., caustics of "diffraction" rays. This is a feature of the hybrid approach of the asymptotic calculation method. More accurate calculations, taking into account diffraction effects, were performed by the method of expansion in conical waves.

Note that the structural (caustic) features of the generated field, especially its longitudinal distribution, are more clearly defined using the asymptotic-geometric approach, and the fine details and distribution in the focal plane are correctly shown by the method of expansion in conical waves. Thus, each of the methods allows you to focus on various features of the generated fields.

Equations of 3D-caustic surfaces were obtained and the conditions for the dependence of the ring radius on the order of the vortex phase singularity awas analyzed. It was shown that, in the non-paraxial regime, during the formation of small light rings (several tens of wavelengths), there is a noticeable influence of the vortex phase singularity. The increase in the radius of the ring will be negligible only for small orders of the vortex phase singularity m ($m < 2\pi/\lambda$), and for large values of m ($m >> 2\pi/\lambda$), the ring will grow linearly with increasing m. In addition, at large values of for a parabolic vortex toroidal lens, a significant displacement of the plane of formation of the annular distribution closer to the plane of the element was found. This effect was less pronounced for a non-paraxial vortex toroidal lens.

The revealed features should be taken into account when using the considered optical elements generating the POV in various applications, such as optical trapping and manipulation, vortex-based multiplexing, and laser structuring.

Author Contributions: Conceptualization, V.A.S., S.N.K., and S.I.K.; methodology, S.N.K., V.A.S., and S.I.K.; software, S.G.V.; validation, S.N.K. and S.I.K.; formal analysis, S.I.K. and S.N.K.; investigation, S.N.K., S.I.K., and S.G.V.; data curation, S.G.V.; writing—original draft preparation, S.N.K., S.I.K., and V.A.S.; writing—review and editing, S.N.K., S.I.K., and V.A.S.; visualization, S.N.K. and S.G.V.; supervision, V.A.S. and S.N.K.; funding acquisition, S.N.K. All authors have read and agreed to the published version of the manuscript.

Funding: This work was partly funded by the Russian Foundation for Basic Research under grant No. 20-07-00505 (numerical calculations) and the Ministry of Science and Higher Education within the government project of FSRC "Crystallography and Photonics" RAS under agreement 007-GZ/Ch3363/26 (theoretical analysis).

Data Availability Statement: Not applicable.

Acknowledgments: The part of calculations were performed on the hybrid supercomputer K-100 installed in the Supercomputer Center of Collective Usage of KIAM RAS.

Conflicts of Interest: The authors declare that there are no conflicts of interest related to this article.

References

1. Ostrovsky, A.S.; Rickenstorff, C.; Arrizón, V. Generation of the "perfect" optical vortex using a liquid-crystal spatial light modulator. *Opt. Lett.* **2013**, *38*, 534–536. [CrossRef]
2. Chen, M.; Mazilu, M.; Arita, Y.; Wright, E.; Dholakia, K. Dynamics of microparticles trapped in a perfect vortex beam. *Opt. Lett.* **2013**, *38*, 4919–4922. [CrossRef]
3. Rickenstorff, C.; García-García, J.; Martínez, A.S.; Ostrovsky, A.S.; Arrizón, V. Generation of the "perfect" vortex for optical trapping. In *Frontiers in Optics*; Delyett, P., Jr., Gauthier, D., Eds.; OSA Technical Digest: Washington, DC, USA, 2013; p. JW3A.34.
4. Vaity, P.; Rusch, L. Perfect vortex beam: Fourier transformation of a Bessel beam. *Opt. Lett.* **2015**, *40*, 597–600. [CrossRef] [PubMed]
5. Phillips, R.L.; Andrews, L.C. Spot size and divergence for Laguerre Gaussian beams of any order. *Appl. Opt.* **1983**, *22*, 643–644. [CrossRef] [PubMed]
6. Curtis, J.E.; Grier, D. Structure of Optical Vortices. *Phys. Rev. Lett.* **2003**, *90*, 133901. [CrossRef]
7. Padgett, M.; Miatto, F.; Lavery, M.; Zeilinger, A.; Boyd, R.W. Divergence of an orbital-angular-momentum-carrying beam upon propagation. *New J. Phys.* **2015**, *17*, 023011. [CrossRef]
8. Zhang, J.; Huang, S.-J.; Zhu, F.-Q.; Shao, W.; Chen, M.-S. Dimensional properties of Laguerre–Gaussian vortex beams. *Appl. Opt.* **2017**, *56*, 3556–3561. [CrossRef] [PubMed]
9. Paterson, C.; Smith, R. Higher-order Bessel waves produced by axicon-type computer-generated holograms. *Opt. Commun.* **1996**, *124*, 121–130. [CrossRef]
10. Arlt, J.; Dholakia, K. Generation of high-order Bessel beams by use of an axicon. *Opt. Commun.* **2000**, *177*, 297–301. [CrossRef]
11. Dudley, A.; Milione, G.; Alfano, R.R.; Forbes, A. All-digital wavefront sensing for structured light beams. *Opt. Express* **2014**, *22*, 14031–14040. [CrossRef] [PubMed]
12. Wei, X.; Liu, C.; Niu, L.; Zhang, Z.; Wang, K.; Yang, Z.; Liu, J. Generation of arbitrary order Bessel beams via 3D printed axicons at the terahertz frequency range. *Appl. Opt.* **2015**, *54*, 10641–10649. [CrossRef]
13. Choporova, Y.Y.; Knyazev, B.A.; Kulipanov, G.N.; Pavelyev, V.; Scheglov, M.A.; Vinokurov, N.A.; Volodkin, B.O.; Zhabin, V.N. High-power Bessel beams with orbital angular momentum in the terahertz range. *Phys. Rev. A* **2017**, *96*, 023846. [CrossRef]
14. Yan, H.; Zhang, E.; Zhao, B.; Duan, K. Free-space propagation of guided optical vortices excited in an annular core fiber. *Opt. Express* **2012**, *20*, 17904–17915. [CrossRef] [PubMed]
15. Kovalev, A.A.; Kotlyar, V.; Porfirev, A.P. A highly efficient element for generating elliptic perfect optical vortices. *Appl. Phys. Lett.* **2017**, *110*, 261102. [CrossRef]
16. Li, D.; Chang, C.; Nie, S.; Feng, S.; Ma, J.; Yuan, C. Generation of elliptic perfect optical vortex and elliptic perfect vector beam by modulating the dynamic and geometric phase. *Appl. Phys. Lett.* **2018**, *113*, 121101. [CrossRef]

17. Li, X.; Ma, H.; Yin, C.; Tang, J.; Li, H.; Tang, M.; Wang, J.; Tai, Y.; Li, X.; Wang, Y. Controllable mode transformation in perfect optical vortices. *Opt. Express* **2018**, *26*, 651–662. [CrossRef]
18. Li, L.; Chang, C.; Yuan, C.; Feng, S.; Nie, S.; Ren, Z.-C.; Wang, H.-T.; Ding, J. High efficiency generation of tunable ellipse perfect vector beams. *Photonics Res.* **2018**, *6*, 1116–1123. [CrossRef]
19. Alonzo, C.A.; Rodrigo, P.J.; Glückstad, J. Helico-conical optical beams: A product of helical and conical phase fronts. *Opt. Express* **2005**, *13*, 1749–1760. [CrossRef]
20. Soifer, V.; Kharitonov, S.; Khonina, S.; Strelkov, Y.; Porfirev, A. Spiral Caustics of Vortex Beams. *Photonics* **2021**, *8*, 24. [CrossRef]
21. Wang, Z.; Yuan, Z.; Gao, Y.; Yan, W.; Liang, C.; Ren, Z.-C.; Wang, X.-L.; Ding, J.; Wang, H.-T. Twin curvilinear vortex beams. *Opt. Express* **2021**, *29*, 14112–14125. [CrossRef]
22. Chen, Y.; Wang, T.; Ren, Y.; Fang, Z.-X.; Ding, G.; He, L.; Lu, R.-D.; Huang, K. Generalized perfect optical vortices along arbitrary trajectories. *J. Phys. D Appl. Phys.* **2021**, *54*, 214001. [CrossRef]
23. Khonina, S.; Porfirev, A. Generation of multi-contour plane curves using vortex beams. *Int. J. Light Electron. Opt.* **2021**, *229*, 166299. [CrossRef]
24. Yu, J.; Zhou, C.; Lu, Y.; Wu, J.; Zhu, L.; Jia, W. Square lattices of quasi-perfect optical vortices generated by two-dimensional encoding continuous-phase gratings. *Opt. Lett.* **2015**, *40*, 2513–2516. [CrossRef]
25. Fu, S.; Wang, T.; Gao, C. Perfect optical vortex array with controllable diffraction order and topological charge. *J. Opt. Soc. Am. A* **2016**, *33*, 1836–1842. [CrossRef] [PubMed]
26. Karahroudi, M.K.; Parmoon, B.; Qasemi, M.; Mobashery, A.; Saghafifar, H. Generation of perfect optical vortices using a Bessel-Gaussian beam diffracted by curved fork grating. *Appl. Opt.* **2017**, *56*, 5817–5823. [CrossRef]
27. Khonina, S.N.; Ustinov, A.V.; Kirilenko, M.S.; Kuchmizhak, A.A.; Porfirev, A.P. Application of a binary curved fork grating for the generation and detection of optical vortices outside the focal plane. *J. Opt. Soc. Am. B* **2020**, *37*, 1714. [CrossRef]
28. Wang, H.; Fu, S.; Gao, C. Tailoring a complex perfect optical vortex array with multiple selective degrees of freedom. *Opt. Express* **2021**, *29*, 10811–10824. [CrossRef] [PubMed]
29. Tkachenko, G.; Chen, M.; Dholakia, K.; Mazilu, M. Is it possible to create a perfect fractional vortex beam? *Optica* **2017**, *4*, 330. [CrossRef]
30. Bianchetti, A.; Etchepareborda, P.; Federico, A. Determining the fractional topological charge shifting in perfect vortices from laser speckle. *Opt. Commun.* **2019**, *441*, 74–79. [CrossRef]
31. Li, P.; Zhang, Y.; Liu, S.; Ma, C.; Han, L.; Cheng, H.; Zhao, J. Generation of perfect vectorial vortex beams. *Opt. Lett.* **2016**, *41*, 2205–2208. [CrossRef]
32. Fu, S.; Wang, T.; Gao, C. Generating perfect polarization vortices through encoding liquid-crystal display devices. *Appl. Opt.* **2016**, *55*, 6501–6505. [CrossRef]
33. Karpeev, S.V.; Paranin, V.D.; Khonina, S.N. Generation of a controlled double-ring-shaped radially polarized spiral laser beam using a combination of a binary axicon with an interference polarizer. *J. Opt.* **2017**, *19*, 055701. [CrossRef]
34. Liang, Y.; Yan, S.; He, M.; Li, M.; Cai, Y.; Wang, Z.; Lei, M.; Yao, B. Generation of a double-ring perfect optical vortex by the Fourier transform of azimuthally polarized Bessel beams. *Opt. Lett.* **2019**, *44*, 1504–1507. [CrossRef]
35. Olvera-Santamaría, M.; García-García, J.; Tlapale-Aguilar, A.; Silva-Barranco, J.; Rickenstorff-Parrao, C.; Ostrovsky, A. Cylindrically polarized perfect optical vortex: Generation and focusing properties. *Opt. Commun.* **2020**, *467*, 125693. [CrossRef]
36. Khonina, S.; Porfirev, A.; Volotovskiy, S.; Ustinov, A.; Fomchenkov, S.; Pavelyev, V.; Schröter, S.; Duparré, M. Generation of Multiple Vector Optical Bottle Beams. *Photonics* **2021**, *8*, 218. [CrossRef]
37. Liang, Y.; Lei, M.; Yan, S.; Li, M.; Cai, Y.; Wang, Z.; Yu, X.; Yao, B. Rotating of low-refractive-index microparticles with a quasi-perfect optical vortex. *Appl. Opt.* **2017**, *57*, 79–84. [CrossRef] [PubMed]
38. Yang, D.; Li, Y.; Deng, D.; Ye, J.; Liu, Y.; Lin, J. Controllable rotation of multiplexing elliptic optical vortices. *J. Phys. D Appl. Phys.* **2019**, *52*, 495103. [CrossRef]
39. Zhu, F.; Huang, S.; Shao, W.; Zhang, J.; Chen, M.; Zhang, W.; Zeng, J. Free-space optical communication link using perfect vortex beams carrying orbital angular momentum (OAM). *Opt. Commun.* **2017**, *396*, 50–57. [CrossRef]
40. Shao, W.; Huang, S.; Liu, X.; Chen, M. Free-space optical communication with perfect optical vortex beams multiplexing. *Opt. Commun.* **2018**, *427*, 545–550. [CrossRef]
41. Karahroudi, M.K.; Moosavi, S.A.; Mobashery, A.; Parmoon, B.; Saghafifar, H. Performance evaluation of perfect optical vortices transmission in an underwater optical communication system. *Appl. Opt.* **2018**, *57*, 9148–9154. [CrossRef]
42. Zhang, C.; Min, C.; Du, L.; Yuan, X.-C. Perfect optical vortex enhanced surface plasmon excitation for plasmonic structured illumination microscopy imaging. *Appl. Phys. Lett.* **2016**, *108*, 201601. [CrossRef]
43. Jabir, M.V.; Chaitanya, N.A.; Aadhi, A.; Samanta, G.K. Generation of "perfect" vortex of variable size and its effect in angular spectrum of the down-converted photons. *Sci. Rep.* **2016**, *6*, 21877. [CrossRef]
44. Syubaev, S.; Zhizhchenko, A.; Vitrik, O.; Porfirev, A.; Fomchenkov, S.; Khonina, S.; Kudryashov, S.; Kuchmizhak, A. Chirality of laser-printed plasmonic nanoneedles tunable by tailoring spiral-shape pulses. *Appl. Surf. Sci.* **2019**, *470*, 526–534. [CrossRef]
45. Qiu, S.; Ren, Y.; Liu, T.; Chen, L.; Wang, C.; Li, Z.; Shao, Q. Spinning object detection based on perfect optical vortex. *Opt. Lasers Eng.* **2020**, *124*, 105842. [CrossRef]
46. Bélanger, P.-A.; Rioux, M. Ring pattern of a lens–axicon doublet illuminated by a Gaussian beam. *Appl. Opt.* **1978**, *17*, 1080–1088. [CrossRef] [PubMed]

47. García-García, J.; Rickenstorff, C.; Ramos-García, R.; Arrizón, V.; Ostrovsky, A.S. Simple technique for generating the perfect optical vortex. *Opt. Lett.* **2014**, *39*, 5305–5308. [CrossRef] [PubMed]
48. Chen, Y.; Fang, Z.-X.; Ren, Y.; Gong, L.; Lu, R.-D. Generation and characterization of a perfect vortex beam with a large topological charge through a digital micromirror device. *Appl. Opt.* **2015**, *54*, 8030–8035. [CrossRef] [PubMed]
49. Kotlyar, V.V.; Kovalev, A.A.; Porfirev, A.P. Optimal phase element for generating a perfect optical vortex. *J. Opt. Soc. Am. A* **2016**, *33*, 2376–2384. [CrossRef]
50. Vasara, A.; Turunen, J.; Friberg, A.T. Realization of general nondiffracting beams with computer-generated holograms. *J. Opt. Soc. Am. A* **1989**, *6*, 1748–1754. [CrossRef]
51. Khonina, S.N.; Kotlyar, V.V. Bessel modes formers. *Proc. SPIE* **1995**, *2363*, 184–190. [CrossRef]
52. Jarutis, V.; Paškauskas, R.; Stabinis, A. Focusing of Laguerre—Gaussian beams by axicon. *Opt. Commun.* **2000**, *184*, 105–112. [CrossRef]
53. Goodell, J.B. Eccentric Lenses for Producing Ring Images. *Appl. Opt.* **1969**, *8*, 2566. [CrossRef] [PubMed]
54. Descour, M.R.; Simon, D.I.; Yeh, W.-H. Ring-toric lens for focus-error sensing in optical data storage. *Appl. Opt.* **1999**, *38*, 1388–1392. [CrossRef] [PubMed]
55. Brzobohaty, O.; Cizmar, T.; Zemánek, P. High quality quasi-Bessel beam generated by round-tip axicon. *Opt. Express* **2008**, *16*, 12688–12700. [CrossRef]
56. Quemener, M.; Guenette, J.; Borne, J.; Thibault, S. Toric lens analysis as a focal ring and Bessel beamgenerator. *J. Opt. Soc. Am. A* **2020**, *37*, 1657–1661. [CrossRef] [PubMed]
57. Selmke, M. Bubble optics. *Appl. Opt.* **2019**, *59*, 45–58. [CrossRef] [PubMed]
58. Xiang, H.; Li, N.; Gao, J.; Zheng, G.; Chen, J.; Wang, C.; Zhuang, S. Comparison and applications of spherocylindrical, toroidal, and ellipsoidal surfaces for the correction of astigmatism in spectacle lenses. *Opt. Express* **2020**, *28*, 1745–1757. [CrossRef]
59. Pinnell, J.; Rodríguez-Fajardo, V.; Forbes, A. How perfect are perfect vortex beams? *Opt. Lett.* **2019**, *44*, 5614–5617. [CrossRef]
60. Khonina, S.N.; Porfirev, A.P. 3D transformations of light fields in the focal region implemented by diffractive axicons. *Appl. Phys. A* **2018**, *124*, 191. [CrossRef]
61. Soifer, V.; Kharitonov, S.I.; Khonina, S.N.; Volotovsky, S.G. Caustics of Vortex Optical Beams. *Dokl. Phys.* **2019**, *64*, 276–279. [CrossRef]
62. Kharitonov, S.I.; Khonina, S.N.; Volotovskiy, S.G.; Kazanskiy, N.L. Caustics of the vortex beams generated by vortex lenses and vortex axicons. *J. Opt. Soc. Am. A* **2020**, *37*, 476–482. [CrossRef] [PubMed]
63. Mansuripur, M. Certain computational aspects of vector diffraction problems. *J. Opt. Soc. Am. A* **1989**, *6*, 786–805. [CrossRef]
64. Khonina, S.N.; Ustinov, A.V.; Kovalev, A.A.; Volotovsky, S.G. Propagation of the radially-limited vortical beam in a near zone. Part I. Calculation algorithms. *Computer Optics* **2010**, *34*, 315–329.
65. Khonina, S.N.; Ustinov, A.V.; Kovalyov, A.A.; Volotovsky, S.G. Near-field propagation of vortex beams: Models and computation algorithms. *Opt. Mem. Neural Netw.* **2014**, *23*, 50–73. [CrossRef]
66. Kravtsov, Y.A.; Orlov, Y.I. *Geometrical Optics of Inhomogeneous Media*; Springer: Berlin/Heidelberg, Germany, 1990; ISBN 978-3-642-84033-3.
67. Born, M.; Wolf, E. *Principles of Optics: Electromagnetic Theory of Propagation, Interference and Diffraction of Light*, 6th ed.; Pergamon Press: Oxford, UK, 1980; ISBN 0-08-026482-4.
68. Poston, T.; Stewart, I. *Catastrophe Theory and Its Applications*; Dover Publication, Inc.: Mineola, NY, USA, 1978; ISBN 0-486-69271-X.
69. Gilmore, R. *Catastrophe Theory for Scientists and Engineers*; Dover: New York, NY, USA, 1993; ISBN 978-0-486-67539-8.
70. Nye, J.F. *Natural Focusing and Fine Structure of Light: Caustics and Wave Dislocations*; Institute of Physics Publishing: Bristol, UK, 1999.
71. Shealya, D.L.; Hoffnagle, J.A. Wavefront and caustic surfaces of refractive laser beam shaper. *Proc. SPIE* **2007**, *6668*, 666805. [CrossRef]
72. Rodrigo, J.A.; Alieva, T.; Abramochkin, E.; Castro, I. Shaping of light beams along curves in three dimensions. *Opt. Express* **2013**, *21*, 20544–20555. [CrossRef]
73. Kharitonov, S.; Volotovsky, S.; Khonina, S. Catastrophe theory and caustics of radially symmetric beams. *Computer Optics* **2019**, *43*, 159–167. [CrossRef]
74. Anguiano-Morales, M.; Martínez, A.; Iturbe-Castillo, M.D.; Chávez-Cerda, S.; Alcalá-Ochoa, N. Self-healing property of a caustic optical beam. *Appl. Opt.* **2007**, *46*, 8284–8290. [CrossRef]
75. Anguiano-Morales, M. Transformation of Bessel beams by means of a cylindrical lens. *Appl. Opt.* **2009**, *48*, 4826–4831. [CrossRef] [PubMed]
76. Cabrera-Rosas, O.D.J.; Espíndola-Ramos, E.; Juárez-Reyes, S.A.; Julián-Macías, I.; Ortega-Vidals, P.; Silva-Ortigoza, G.; Silva-Ortigoza, R.; Sosa-Sánchez, C.T. Wavefronts and caustic associated with Durnin's beams. *J. Opt.* **2016**, *19*, 015603. [CrossRef]
77. Sosa-Sánchez, C.T.; Silva-Ortigoza, G.; Juárez-Reyes, S.A.; Cabrera-Rosas, O.D.J.; Espíndola-Ramos, E.; Julián-Macías, I.; Ortega-Vidals, P. Parabolic non-diffracting beams: Geometrical approach. *J. Opt.* **2017**, *19*, 085604. [CrossRef]
78. Julián-Macías, I.; Rickenstorff, C.; Cabrera-Rosas, O.D.J.; Espíndola-Ramos, E.; Juárez-Reyes, S.A.; Ortega-Vidals, P.; Silva-Ortigoza, G.; Sosa-Sánchez, C.T. Wavefronts and caustics associated with Mathieu beams. *J. Opt. Soc. Am. A* **2018**, *35*, 267–274. [CrossRef]

79. Zannotti, A.; Denz, C.; Alonso, M.A.; Dennis, M.R. Shaping caustics into propagation-invariant light. *Nat. Commun.* **2020**, *11*, 1–7. [CrossRef]
80. Alonso, M.A.; Dennis, M.R. Ray-optical Poincaré sphere for structured Gaussian beams. *Optica* **2017**, *4*, 476–486. [CrossRef]
81. Dennis, M.R.; Alonso, M.A. Gaussian mode families from systems of rays. *J. Physics Photonics* **2019**, *1*, 025003. [CrossRef]
82. Greenfield, E.; Segev, M.; Walasik, W.; Raz, O. Accelerating Light Beams along Arbitrary Convex Trajectories. *Phys. Rev. Lett.* **2011**, *106*, 213902. [CrossRef]
83. Froehly, L.; Courvoisier, F.; Mathis, A.; Jacquot, M.; Furfaro, L.; Giust, R.; Lacourt, P.A.; Dudley, J.M. Arbitrary accelerating micron-scale caustic beams in two and three dimensions. *Opt. Express* **2011**, *19*, 16455–16465. [CrossRef] [PubMed]
84. Chremmos, I.D.; Chen, Z.; Christodoulides, D.N.; Efremidis, N.K. Abruptly autofocusing and autodefocusing optical beams with arbitrary caustics. *Phys. Rev. A* **2012**, *85*, 023828. [CrossRef]
85. Berry, M.V. Stable and unstable Airy-related caustics and beams. *J. Opt.* **2017**, *19*, 055601. [CrossRef]
86. Ustinov, A.; Khonina, S. Properties of off-axis caustics of autofocusing chirp beams. *Computer Optics* **2020**, *44*, 721–727. [CrossRef]
87. Chen, R.-P.; Chen, Z.; Chew, K.-H.; Li, P.-G.; Yu, Z.; Ding, J.; He, S. Structured caustic vector vortex optical field: Manipulating optical angular momentum flux and polarization rotation. *Sci. Rep.* **2015**, *5*, 10628. [CrossRef] [PubMed]
88. Kharitonov, S.I.; Volotovsky, S.G.; Khonina, S.N. Hybrid asymptotic method for analyzing caustics of optical elements in the axially symmetric case. *Computer Optics* **2017**, *41*, 175–182. [CrossRef]
89. Kharitonov, S.I.; Volotovsky, S.G.; Khonina, S.N.; Kazanskiy, N.L. Diffraction catastrophes and asymptotic analysis of caustics from axisymmetric optical elements. *Proc. SPIE* **2019**, *11146*, 111460K. [CrossRef]
90. Kravtsov, A.Y.; Orlov, Y.I. Caustics, catastrophes, and wave fields. *Sov. Phys. Usp.* **1983**, *26*, 1038–1058. [CrossRef]
91. Borovikov, V.A.; Kinber, B.Y. *Geometrical Theory of Diffraction*; The Institution of Electrical Engineers: London, UK, 1994; ISBN 0-85296-830-2.
92. Keller, J.B. Geometrical theory of diffraction. *J. Opt. Soc. Am.* **1962**, *52*, 116–130. [CrossRef]